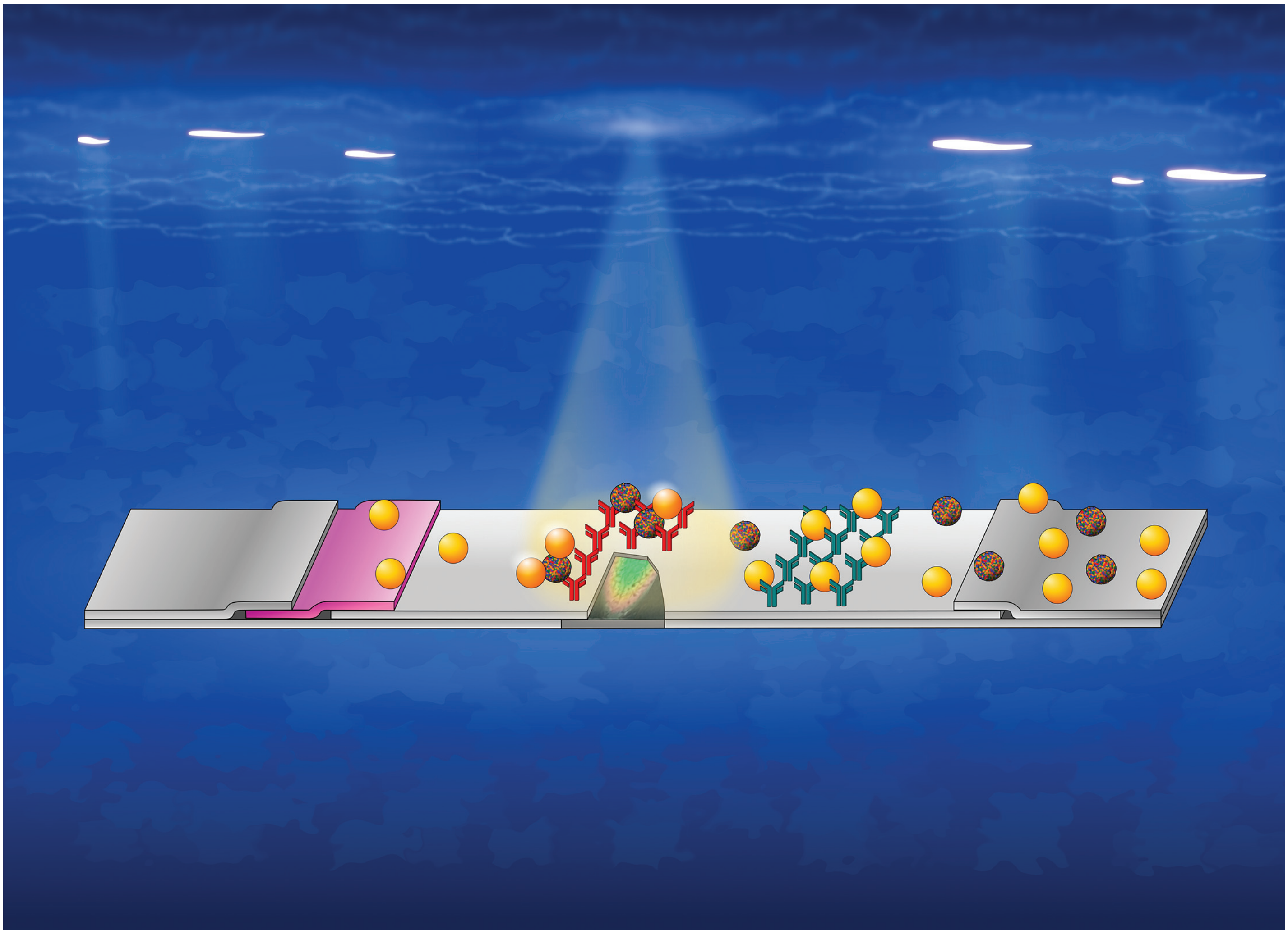

Showcasing research from Prof. Nguyen Thi Kim Thanh's laboratory, Biophysics Group, Department of Physics and Astronomy, University College London, UK.

Development of a thermochromic lateral flow assay to improve sensitivity for dengue virus serotype 2 NS1 detection

A lateral flow assay is combined with photothermal nanoparticles and thermochromic sheet for the detection of recombinant dengue virus serotype 2 NS1 protein. By optically stimulating nanoparticles, their temperature is raised and thus being sensed by thermochromic sheet, which results in coloured visual signal. This thermal sensing-based technique is cost-effective and shows significant sensitivity enhancement.

As featured in:

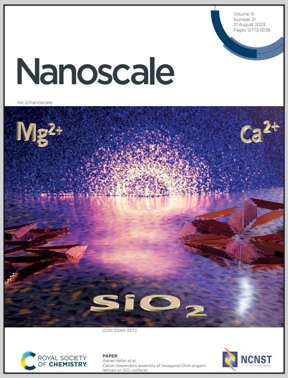

See Nguyen Thi Kim Thanh *et al.*, *Nanoscale*, 2023, **15**, 12915.

ROYAL SOCIETY
OF **CHEMISTRY**

rsc.li/nanoscale

Nanoscale

PAPER

View Article Online
View Journal | View Issue

Cite this: *Nanoscale*, 2023, **15**, 12915

Development of a thermochromic lateral flow assay to improve sensitivity for dengue virus serotype 2 NS1 detection†

Thithawat Trakoolwilaiwan,[a,b] Yasuhiro Takeuchi,[c,d] Terence S. Leung,[e] Matej Sebek,[a,b,f] Liudmyla Storozhuk,[a,b] Linh Nguyen,[g] Le Duc Tung[a,b] and Nguyen Thi Kim Thanh *[a,b]

Received 21st April 2023,
Accepted 13th June 2023

DOI: 10.1039/d3nr01858j

rsc.li/nanoscale

Dengue disease is a viral infection that has been widespread in tropical regions, such as Southeast Asia, South Asia and South America. A worldwide effort has been made over a few decades to halt the spread of the disease and reduce fatalities. Lateral flow assay (LFA), a paper-based technology, is used for dengue virus detection and identification because of its simplicity, low cost and fast response. However, the sensitivity of LFA is relatively low and is usually insufficient to meet the minimum requirement for early detection. In this study, we developed a colorimetric thermal sensing LFA format for the detection of dengue virus NS1 using recombinant dengue virus serotype 2 NS1 protein (DENV2-NS1) as a model antigen. Plasmonic gold nanoparticles, including gold nanospheres (AuNSPs) and gold nanorods (AuNRs), and magnetic nanoparticles (MNPs), namely iron oxide nanoparticles (IONPs) and zinc ferrite nanoparticles (ZFNPs), were studied for their thermal properties for sensing assays. AuNSPs with 12 nm diameter were chosen due to their great photothermal effect against light-emitting diodes (LEDs). In the thermal sensing assay, a thermochromic sheet is used as a temperature sensor transforming heat into a visible colour. In the typical LFA, the test line is visible at 6.25 ng mL^{-1} while our thermal sensing LFA offers a visual signal that can be observed at as low as 1.56 ng mL^{-1}. The colorimetric thermal sensing LFA is capable of reducing the limit of detection (LOD) of DENV2-NS1 by 4 times compared to the typical visual readout. The colorimetric thermal sensing LFA can enhance the sensitivity of detection and deliver visuality to the user to translate without the need for an infrared (IR) camera. It has the potential to expand the utilities of LFA and satisfy early diagnostic applications.

1. Introduction

Dengue fever is a mosquito-borne disease that can cause degrees of acute symptomatic illness from mild to life-threatening conditions in infected patients. There are four antigenically different serotypes of dengue virus (DENV) namely DENV1, DENV2, DENV3 and DENV4.[1] The most prevalent serotype contributing to dengue infection is DENV2.[2]

The number of DENV infection cases has grown over the last two decades.[3,4] There are approximately 390 million cases of DENV infection in the world every year and only 25% of them have apparent symptoms of dengue illness. The disease has been contagiously spread across tropical regions, particularly in Asia.[2,3,5] Dengue infection has an adverse impact on global health and extra awareness is needed to control, provide surveillance and avoid the expansion of endemic DENV.

Current methods to monitor DENV infection involve virological and serological tests to identify the presence of viral components or immune components through which the human

---

[a] *Biophysics Group, Department of Physics and Astronomy, University College London, Gower Street, London, WC1E 6BT, UK. E-mail: ntk.thanh@ucl.ac.uk;* **https://ntk-thanh.co.uk**

[b] *UCL Healthcare Biomagnetics and Nanomaterials Laboratories, 21 Albemarle Street, London, W1S 4BS, UK*

[c] *Division of Infection and Immunity, University College London, UK*

[d] *Biotherapeutics and Advanced Therapies, Scientific Research and Innovation, Medicines and Healthcare Products Regulatory Agency, South Mimms, UK*

[e] *Department of Medical Physics and Biomedical Engineering, University College London, UK*

[f] *Institute of Materials Research and Engineering, Agency for Science, Technology and Research (A*STAR), 2 Fusionopolis Way, #08-03, Innovis, Singapore 138634, Singapore*

[g] *Division of Biomaterials and Tissue Engineering, UCL Eastman Dental Institute, University College London, UK*

† Electronic supplementary information (ESI) available. See DOI: **https://doi.org/10.1039/d3nr01858j**

body builds up resistance against viral infection.[3,7–9] Commonly, nucleic acids extracted from whole blood, serum, or plasma are amplified using a reverse transcription-polymerase chain reaction. On the other hand, a serological-based analysis seeks an antibody produced by the immune system in response to DENV. These analyses are highly specific and sensitive, yet they need to be handled by specialists, advanced laboratory equipment and expensive reagents. An alternative simple and rapid LFA test kit has been clinically utilized for detection of antigenic biomarkers, *i.e.* viral NS1 proteins.[9] It was found that a paper-based assay is specific to the dengue virus, but the sensitivity needs to be improved to detect low levels of NS1 in the body. Hence, the outcome of LFA is usually confirmed by other standard methods to obtain a conclusive result. This limits the utility of LFA to be used in early diagnosis.

To address the existing issues with LFA, there have been several approaches to enhance its sensitivity, *e.g.* increasing the number of the binding sites on gold nanoparticles, that was designed to sit on a large silica substrate,[10] dual attachment of the labelling nanoparticles,[11] inducing a chemical catalytic reaction,[12–14] image processing[15] and magnetization measurement.[16] Recent studies have exploited the use of photothermal nanoparticles in biosensing assays in which heat measurement can be achieved by monitoring either irradiation using an IR camera[17–21] or the conduction of heat.[17,22] Other studies have reported the potential of using thermally sensitive material in biosensing applications based on the conversion of heat into a visual signal to enable a naked eye interpretation.[23,24]

To the best of our knowledge, liquid crystal thermochromic materials have never been integrated into an LFA system. We developed a colorimetric thermal sensing LFA to detect DENV2-NS1, the protein secreted from DENV2-infected cells. The visual signals received from the test line of a typical LFA and thermochromic signal intensity are compared in this study. Various photothermal nanoparticles, including MNPs and plasmonic nanoparticles, were investigated in this study to find the optimal nanoheater for the assay. They were illuminated with multi-wavelength light provided by an LED. The selected particles were used as visual signal providers for a typical LFA and as a light-to-heat converter for the thermal sensing assay. A liquid crystal thermochromic sheet served as a thermal sensor to display detectable coloration. The duration and power intensity of illumination were also optimized in this study. Quantification was determined by the use of customized MATLAB code.[25]

2. Materials and methods

2.1 Materials

Chemical reagents to fabricate nanoparticles including iron(III) acetylacetonate ($Fe(acac)_3$, ≥99.9% trace metals basis), zinc acetylacetonate hydrate ($Zn(acac)_2$, 99.995% trace metals basis), triethylene glycol (TREG, ReagentPlus®, 99%), trisodium citrate dihydrate, gold(III) chloride solution ($HAuCl_4$, 99.99% trace metals basis), borate buffer, sucrose, sodium chloride (NaCl), potassium carbonate (K_2CO_3), hexadecyl trimethylammonium bromide (CTAB, for molecular biology, ≥99%), silver nitrate ($AgNO_3$, ACS reagent, ≥99.0%), sodium borohydride ($NaBH_4$, ReagentPlus®, 99%), L-ascorbic acid, sodium bromide (NaBr, ACS reagent, ≥99.0%), sodium nitrate ($NaNO_3$, ReagentPlus®, ≥99.0%) and bovine serum albumin (BSA) were received from Sigma Aldrich (UK). HCl (37%) was purchased from Acros Organics (UK). Deionized (DI) water was used for all syntheses and redispersion of AuNSPs. All glassware and magnetic stir bars were cleaned with aqua regia to remove any residual gold traces and dried in an oven before each use. Thermal sensing LFA components were supplied as described in the following. A Whatman FF170HP nitrocellulose membrane and backing card were obtained from GE Healthcare Life Sciences (UK). Sample and absorbent pads were bought from Merck (UK). Biological components, including mouse anti-dengue virus pan-serotype NS1 antibody EA1 (mAb, product code: MAB12295), rabbit anti-dengue virus pan-serotype NS1 polyclonal antibody (pAb, product code: PAB21481), goat anti-mouse IgG (product code: PAB21441) and recombinant dengue virus serotype 2 NS1 protein (HEK293, product code: DENV2-NS1), were produced by The Native Antigen Company (UK). Phosphate buffered saline (PBS) was acquired from Gibco (UK). A 30–35 °C liquid crystal thermochromic colour-changing sheet was obtained from SFXC (UK). A white warm light-emitting diode (LED), with wavelengths of 400 to 700 nm (Fig. S1A†), was purchased from Thorlabs (UK).

2.2 Synthesis and characterization

2.2.1 Synthesis of MNPs. Polyol-capped IONPs and ZFNPs were produced based on the polyol-based method.[26] The precursor for IONP synthesis was prepared by mixing vigorously 4 mmol of $Fe(acac)_3$ in 20 ml of TREG, followed by 2 h of sonication. The protocol has been slightly modified to yield zinc-doped ferrite nanoparticles with polyol coating. To prepare zinc ferrite precursor, 174 mM of $Fe(acac)_3$ and 26 mM of $Zn(acac)_2$ were added to a tube containing 20 mL of TREG solution followed by vortex mixing and sonication for 2 h.

Both metal precursor solutions were transferred to 45 mL capacity Teflon liners, which were later loaded into alloy steel autoclave jackets. Their tops were closed by PTFE gaskets and sealed with screw caps before placing them in an oven (Memmert, model UFP400). The program was pre-set to immediately increase the temperature to 250 °C and maintained at this point for 8 h then ramping down to 20 °C and being held for 2 h. The excess solvent and by-products were removed by magnetic separation in acetone and DI water. The washing process was performed twice. Black pellets were retrieved and redispersed in DI water.

Then, trisodium citrate was added to the dispersion to reach 1000 mM and the mixture was gently shaken on a rotator mixer for 24 h at room temperature (RT). Unbound TREG and citrate in the aqueous solution were removed using a permanent magnet and rinsed several times with acetone and DI water. The final products were dispersed in water.

2.2.2 Synthesis of AuNSPs. Spherical gold nanoparticles were reproduced according to a previous study.[27] Briefly, 50 mL of 0.03 wt% $HAuCl_4$ was boiled followed by the addition of 2.5 and 5 mL of trisodium citrate (1 wt%) with continuous stirring. The light-yellow solution turned to dark purple and eventually to ruby, indicating the success of the reaction. AuNSP solutions were left for 10 min at boiling point under stirring before the heat was removed. The solution was still continuously stirred at RT for another 20 min to ensure the completion of the reaction.

2.2.3 Synthesis of AuNRs. Rods with different aspect ratios were reproduced from the literature.[28,29] The seed solution was formed by preparing a 10 mL mixture of 0.25 mM $HAuCl_4$ and 0.1 M CTAB. Subsequently, 0.6 mL of fresh ice-cold $NaBH_4$ (10 mM) was injected into the mixture. It was vigorously stirred and left undisturbed for 1 h to age the growth of gold seeds.

Second, 5 mL of 1.4 mM $HAuCl_4$ was mixed with 5 mL of 0.2 M CTAB to prepare the growth solution. Then, different volumes (75, 100 and 125 μL) of 10 mM $AgNO_3$ were added to the growth solution. This was followed by the addition of 1.25 M NaBr (0.25 mL) and 37% HCl (10 μL). Next, 79 mM of L-ascorbic acid (105 μL) was injected quickly and the mixture stirred for 30 s until it became colourless. During this step, the growth solution was formed.

Then, the freshly prepared growth solution was mixed with 60 μL of the seed solution. The mixture was incubated at 30 °C overnight to grow AuNRs. The particles were purified by centrifugation (8500 rpm) for 20 min. The supernatant was discarded, and the pellets were redispersed in water. Rod-shaped plasmonic nanoparticles were selected for use in the investigation due to their excellent photothermal properties.

2.2.4 Characterization. The morphology of the nanoparticles was revealed by transmission electron microscopy (TEM) at an accelerating voltage of 120 kV using a JEOL-1200 EX microscope with Gatan DigitalMicrograph software. The diameter and size distribution were determined using the free software ImageJ. Absorption spectra of the colloidal nanoparticles were obtained using ultraviolet-visible (UV-Vis) spectroscopy (SpectraMax M2, molecular device).

2.3 Thermal measurement

All colloidal particles were dispersed in water and adjusted to concentrations of 0.5, 1.0, 1.5 and 2.0 mg mL^{-1}. They were printed on the nitrocellulose membrane at 0.1 and 0.2 μL mm^{-1} using a bioreagent dispenser (Claremont BioSolutions LLC, Upland, CA). The pre-deposited nitrocellulose membranes were illuminated with a power intensity of 6.5 W cm^{-2} for 3 min. The temperature change was recorded using a thermal imager (Testo 875i) and was analyzed using "Testo IRsoft" software. The configurative setup for this thermal measurement is displayed in Fig. 1. A bare membrane was used as a negative control. Temperature measurement was performed in triplicate. The temperature gradient was determined as follows:

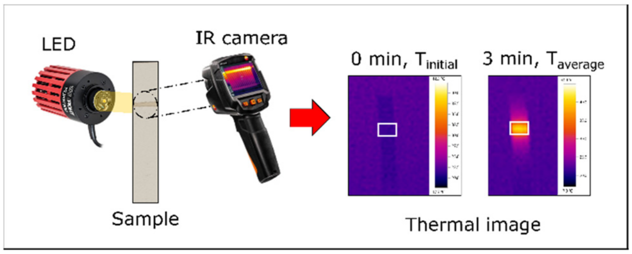

Fig. 1 A diagram of thermal measurement. Nanoparticles on the nitrocellulose membrane are illuminated with an LED. Thermal recording is achieved using an IR camera.

$$\Delta T = T_{\text{average}} - T_{\text{initial}} \qquad (1)$$

where ΔT is the gradient of temperature, T_{average} is the average temperature of the test line and T_{initial} is the initial temperature of the membrane before illumination.

2.4 Aggregation assay and preparation of AuNSP@mAb

The conjugation protocol of antibody-conjugated AuNSPs (AuNSP@mAb) was optimized using a salt-induced aggregation assay, called a flocculation test. To find the optimum conditions for the antibody binding of AuNSPs, the pH of the as-synthesised gold colloid with an optical density at 520 nm wavelength (OD_{520}) of 1.0 was altered using 0.1M K_2CO_3 over a range between 6.5 and 9.5 with 0.5 unit intervals. 200 μL of dispersion at each pH was transferred to a 96-well plate to which 10 μL of mAb was added to reach a final concentration of 20 μg mL^{-1}. The dispersion was vigorously mixed at RT for 30 min and 20 μL of 10% NaCl was then added to disturb the stability of the conjugates. After 10 min of incubation, the absorption was measured at wavelengths of 520 and 650 nm.

The ideal pH at which the dispersion was stable from the above experiment was chosen to determine the optimum antibody concentration. The mAb was added to interact with 200 μL of the as-synthesized AuNSPs (OD_{520} = 1.0 and pH 9.0) in a 96-well plate with the final concentrations ranging from 5 to 20 μg mL^{-1}. The conjugates were kept under continuous rotation for 30 min at RT. This was followed by the addition of 20 μL of 10% NaCl and mixing for 10 min. The absorption spectrum of the conjugate was measured at 520 nm and 650 nm.

AuNSP@mAb for LFA operation was prepared based on the optimum conditions determined from the aggregation assay. The colloidal dispersion of AuNSPs (OD_{520} = 1.0) was centrifuged and adjusted to pH 9.0 using 0.1 M K_2CO_3. Following this, the colloid was vigorously mixed with mAb at a final concentration of 10 μg mL^{-1} for 30 min. The conjugate was then blocked with 1% BSA for 30 min. Unbound mAb and BSA were removed by centrifugation at 14 000 rpm for 20 min at 4 °C. The washing step was repeated twice. The pellets were redispersed in the conjugate pad buffer (20 mM borate buffer, pH

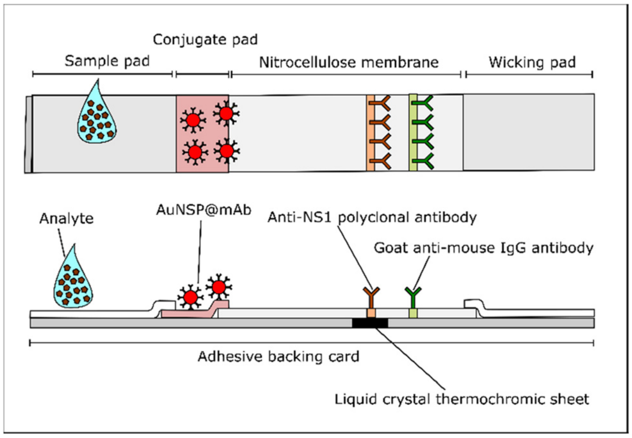

Fig. 2 The architecture of the colorimetric thermal sensing LFA. It is composed of a sample pad, a conjugate pad, a nitrocellulose membrane, test and control lines, a wicking pad, and a thermochromic sheet.

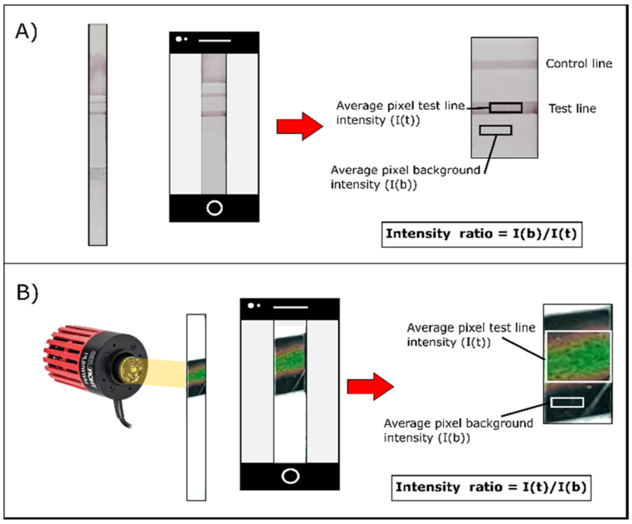

Fig. 3 Schemes represent the image acquisition and calculation of the visual intensity ratio signal for (A) a typical visual assay and (B) a colorimetric thermal sensing assay. The colour intensity is quantified by image processing. The contrast of the typical visual readout can be obtained by dividing the colour intensity of the background by that of the test line. Inversely, the contrast of thermal visual signals is calculated by determining the ratio of the thermochromic signal to the colour intensity of the thermochromic sheet.

9.0 supplemented with 1% BSA, 0.5% Tween 20, and 5% sucrose) and stored at 4 °C until use.

2.5 Fabrication of thermochromic LFA

The components of the colorimetric thermal sensing LFA are displayed in Fig. 2. It comprises similar parts to a general LFA with the integration of a liquid crystal thermochromic sheet. The nitrocellulose membrane (25 mm) was dispensed with 0.5 mg $\mathrm{mL^{-1}}$ of pAb (test line) and 0.3 mg $\mathrm{mL^{-1}}$ of goat anti-mouse IgG (control line) at 0.1 $\mu\mathrm{L\ mm^{-2}}$ using an automated lateral flow reagent dispenser (Claremont BioSolution LLC, Upland, CA). Antibodies were prepared in 10 mM PBS with 5% methanol to compromise the fixation of antibodies on the nitrocellulose membrane. A glass fiber conjugate pad (6 mm) was soaked with AuNSP@mAb solution for 30 min and left to dry overnight at RT. All components were assembled on an adhesive backing card with a 2 mm overlap between adjacent parts. A thermochromic sheet (5 mm) was attached under the area of the test line. The assembly was cut into 4 mm widths manually and stored in a desiccator at 4 °C until use.

2.6 Optimization of power intensity and length of illumination

The concentration of DENV2-NS1 was adjusted to 0.78, 1.5, 12.5 and 100 ng $\mathrm{mL^{-1}}$ in sample buffer (10 mM PBS, 0.5% BSA, and 0.1% Tween 20). 100 µL of the spiked sample was added to the thermochromic adhered strips. They were illuminated using an LED with power intensities of 5.2, 6.5 and 8.16 W $\mathrm{cm^{-2}}$ for 10 to 60 s, then the images of the thermochromic sheets were taken. The experiment was operated at 22 °C.

2.7 Assay procedures of typical and thermochromic LFA

DENV2-NS1 was prepared in a series of two-fold serial dilutions ranging from 0.78 to 400 ng $\mathrm{mL^{-1}}$ in a sample buffer (10 mM PBS, 0.5% BSA, and 0.1% Tween 20). Then, 100 µL of the diluent was transferred to the sample pad and the solution migrated through the strip by capillary force. The antigenic interaction between the AuNSP@mAb and DENV2-NS1 forms visible lines on the strip, whereas unreacted AuNSP@mAb and DENV2-NS1 were destined for the wicking pad. All experiments were performed in triplicate. Quantification of the typical visual signal and thermochromic signal is shown in Fig. 3. To obtain a typical visual signal contrast, images of the detection zone were acquired using a mobile phone to determine a quantification curve (Fig. 3A). After the completion of the conventional assay, the test line was illuminated using an LED light at 6.5 W $\mathrm{cm^{-2}}$ for 30 s. The photographs of the thermochromic sheet were immediately taken after turning off the LED using a mobile phone (Samsung Galaxy S9+) (Fig. 3B). Camera configurations (distance between object and camera, focal length, shutter speed, flash, and ISO: the level of sensitivity to illuminated light) were kept constant to eliminate external interference. The colour intensity of the signal was quantified by image processing using optimized MATLAB code with minimal effect of external light reflections.[25] The analytical performance (sensitivity and the LOD) was assessed. The sensitivity is represented by the slope of the linear regression equation. To find the detection limit of the signal, the International Union of Pure and Applied Chemistry (IUPAC) method (eqn (2)) was used to determine the minimum signal that is distinguishable from the blank sample:[17–19,30]

$$S_{\mathrm{LOD}} > S_{\mathrm{B}} + 3 \times \sigma_{\mathrm{B}} \tag{2}$$

where S_{LOD} is the LOD of the signal, S_{B} is the mean of the signal received from the blank samples and σ_{B} is the standard deviation of blank samples.

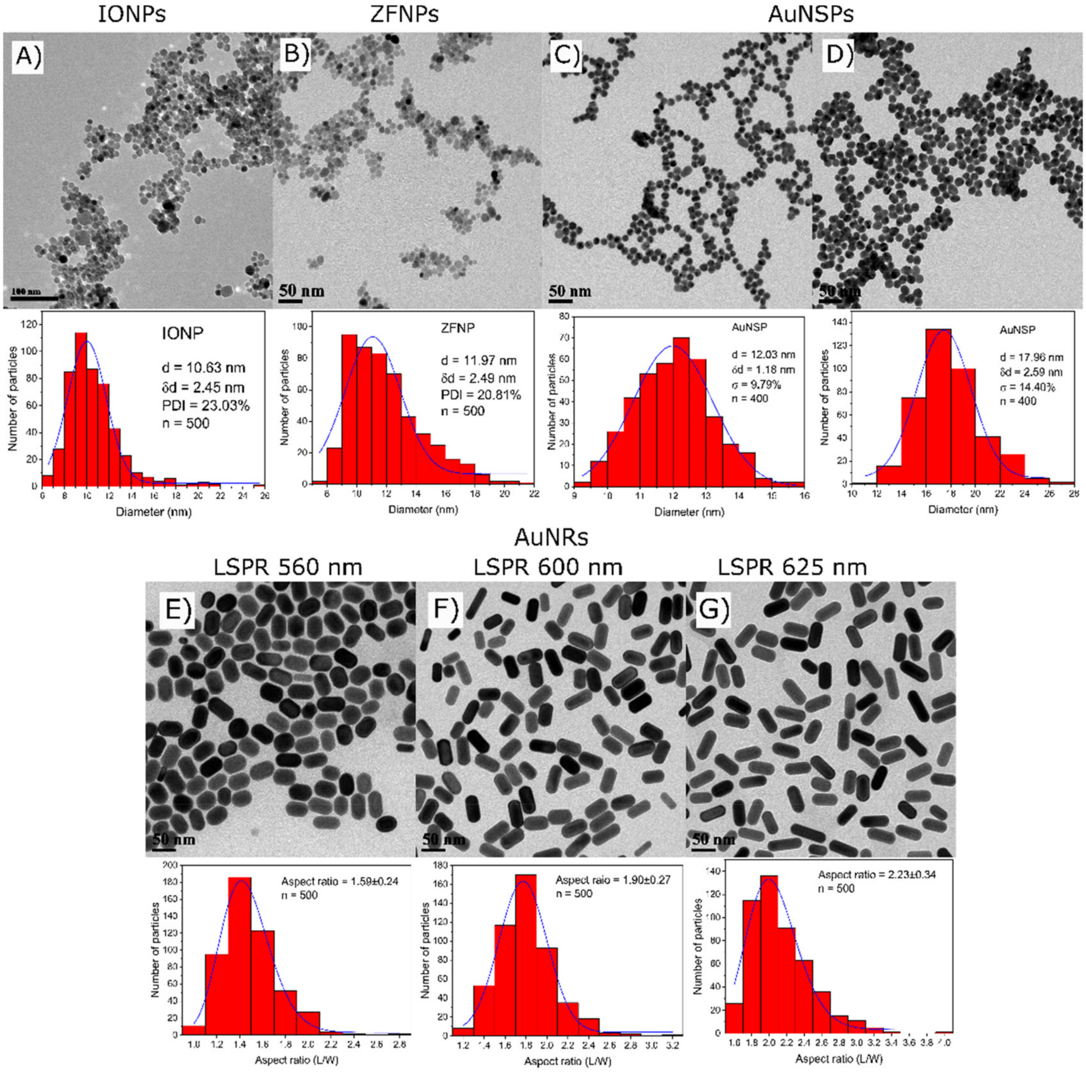

Fig. 4 TEM images and size distributions of MNPs and plasmonic nanoparticles. The top row represents the morphological information of (A) IONPs, (B) ZFNPs, (C) AuNSPs to which is added 5 mL of trisodium citrate and (D) AuNSPs to which is added 2.5 mL of trisodium citrate. The bottom panel displays the morphology and aspect ratio of AuNRs to which different volume of 10 mM $AgNO_3$ is added (E) 75 µL, (F) 100 µL and (G) 125 µL.

3. Results and discussion

3.1 Characterization studies

The morphological information on the nanoparticles was acquired by TEM as shown in Fig. 4. The MNPs are spherical 10.6 nm IONPs (Fig. 4A) and 12.0 nm ZFNPs (Fig. 4B). The diameters of AuNSPs are tunable depending on the volume of the added reductant. AuNSPs with a diameter of 12.0 nm were obtained with the addition of 5 mL of 1 wt% trisodium citrate (Fig. 4C), while 18.0 nm AuNSPs were produced by adding 2.5 mL of trisodium citrate (Fig. 4D). Histograms are shown alongside TEM images to represent the polydispersity of each nanomaterial. For the rod-shaped gold nanoparticles, by varying the volume of silver nitrate addition, the dimension of AuNRs can be tailored (Fig. 4E–G). The length of the rod was varied from 49 to 55 nm, whilst the width was between 31 and 25 nm. The aspect ratio of the rods is between 1.59 and 2.23.

Absorption spectra of all nanoparticle suspensions at 0.05 mg mL^{-1} in DI water were measured from 400 to 800 nm using a SpectraMax M2e. The MNPs have brown/black colour and absorb mostly in the shorter wavelength of the blue region (Fig. S1B†). The absorption intensity decreases at longer wavelengths where least absorption falls in the red region of the spectrum. In contrast, the plasmonic nanoparticles exhibited different optical patterns. Maximum light absorption was centered at 517 and 522 nm for the small and large AuNSPs, respectively. For AuNRs, two absorption peaks were observed, corresponding to the longitudinal and transverse peaks being the more intense and less intense peak, respectively. They exhibit different localized surface plasmon resonances (LSPRs) depending on their aspect ratios. AuNRs exhibit longitudinal LSPR peaks at 560, 600 and 625 nm for 75, 100 and 125 µL of silver nitrate (10 mM) added in the syntheses, respectively. The increase of silver nitrate concentration causes a red shift in the

LSPR band and enhances the intensity, corresponding to the higher aspect ratio.[28,29]

3.2 Thermal measurement

The thermal properties of the nanoparticles were investigated using a broad-spectrum LED. To identify the most effective nanoparticles, their light-to-heat conversion capability on nitrocellulose membranes was investigated using an IR camera. In Fig. 5, ZFNPs were able to produce temperatures up to 25 °C at 2.0 mg mL^{-1} at a dispensing rate of 0.2 μL mm^{-1} whilst IONPs only raised the temperature up to 18 °C. This shows that at the highest dispensing rate, the nanoparticles exhibit the strongest photothermal activity. Moreover, it was observed that the most diluted concentration of IONPs and ZFNPs can raise the temperature distinctly above the temperature of the nanoparticle-free nitrocellulose membrane, emphasizing their great photothermal conversion performances toward white light.

Two different sizes of citrate-capped AuNSPs (12 and 18 nm diameters) were subjected to a photothermal experiment. Upon illumination, the temperature of the larger AuNSPs was not distinguishable from the null signal of the illuminated nitrocellulose membrane. The 12 nm AuNSPs reached a maximum temperature difference of 16.9 °C, being comparable to that of IONPs (17.0 °C), but less than that of ZFNPs (24.9 °C). The AuNRs with the LSPR at 560 nm were unable to raise the temperature above the threshold of background noise. To maximise the optical properties of the nanorods here, the aspect ratios were tuned to centralise the LSPR peaks at around 600 and 625 nm, which are around the region of the highest intensity provided by the LED (Fig. S1A†). The nanorods with the highest aspect ratio have stronger photothermal activity than those with the smaller ones, in terms of heat production, whilst being excited using a broad-spectrum LED. Nanorods with medium aspect ratio having maximum absorption at 600 nm raised the temperature by 14 °C while nanorods with maximum absorption at 625 nm could increase the temperature by about 13 °C at 2 mg mL^{-1} (at the highest dispensing rate). The temperature of photo-excited nanoparticles is higher when they were deposited on the membrane at higher dispensing rate, due to the higher number of nanoparticles subjected to LED light.

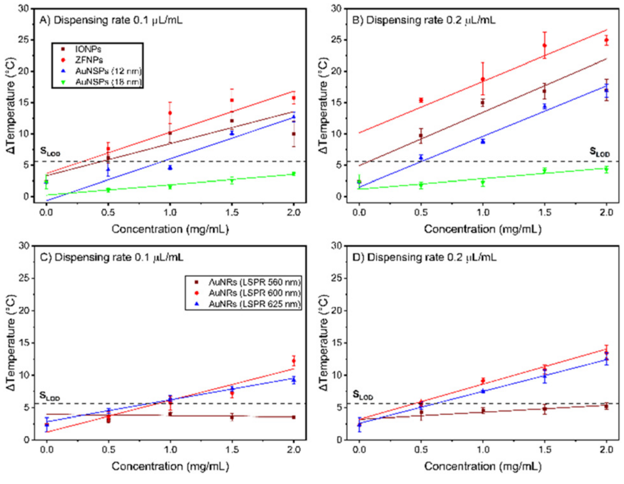

Fig. 5 (A) and (B) Relationships between the temperature gradients and mass concentrations of IONPs, ZFNPs, 12 nm AuNSPs and 18 nm AuNSPs at different dispensing rates and (C) and (D) those of AuNRs with different aspect ratios.

ZFNPs show the highest temperature increase (24.9 °C) compared to other materials in this study. The resulting temperature is affected by the total amount of heat energy, the heat transfer process and the thermal conductivity of nanoparticles.[31] Heat generation is larger when the collective effect of nanoparticles is taken into account, which is governed by the number density of the nanoparticles (eqn 3). When the mass concentration is 0.5 mg mL^{-1}, the particle number concentrations of ZFNPs and 12 nm AuNSPs are 1.04 × 10^{14} particles per mL and 2.84 × 10^{13} particles per mL, respectively. At a dispensing rate of 0.1 μL mm^{-1} and the same light intensity, 12 nm AuNSPs can raise the temperature to a similar level when compared to that of ZFNPs, even though they have 3.7 times fewer nanoparticles. Therefore, in this study, the 12 nm AuNSPs were chosen as the heat provider for the initial development of thermochromic LFA.

3.3 Aggregation assay

The conjugation is subjected to hydrophobic interaction and electrostatic attraction between the positively charged mAb and negatively charged AuNSPs.[32–34] As the surface charge depends on the pH of the solution, it is important to find the appropriate pH value that can stabilize AuNSP@mAb in the presence of electrolytes. It can be seen that a decrease in the pH value tends to develop an aggregation of the conjugate (Fig. 6A). In the test, an excess amount of mAb was added to the solution to ensure sufficient antibody coverage. A basic pH of 9.0 is found to be the favoured point for conjugation to take place as it provides the most stability. The flocculation test continued with a chosen pH of 9.0 to identify the minimum amount of mAb to build a protective layer preventing aggregation (Fig. 6B). In the absence of mAb, the AuNSPs could not tolerate salt destabilization. The conjugate begins to plateau at a final concentration of 10 μg mL^{-1} of mAb. This concen-

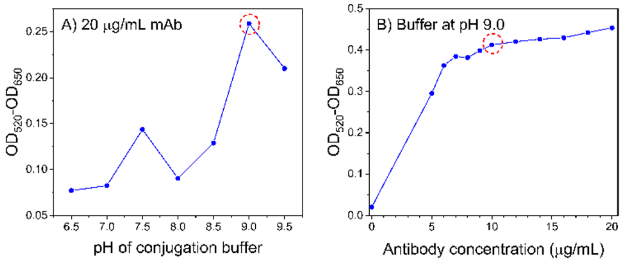

Fig. 6 Aggregation tests for AuNSP@mAb conjugation. (A) The effect of pH and (B) the effect of antibody concentration.

tration is the minimum at which it can stabilize the conjugate by steric repulsion.

It should be noted that antibody coupling by electrostatic force is weak and they are prone to detach in certain environments. This could lead to an aggregation of the AuNSP@mAb, as a result, the capture efficiency decreases because the binding sites are unavailable.[35] Overcoating the antibody is also found to be unfavourable because of high non-specific binding.[19] This emphasizes the necessity to determine the optimal dose of antibodies used as it affects the antigen-capturing activity. However, since different types of antibodies have different morphological structures, an empirical test is therefore required to find the critical conditions for the conjugate to maximize the performance of AuNSP@mAb in each study. It is shown that the antibody attachment in this study reaches an optimum in a solution at pH 9.0 and the concentration of added mAb at 10 μg mL^{-1}.

3.4 Optimization of power intensity and length of illumination

Images of the activated thermochromic sheet are shown in Fig. 7. The strongest power intensity of 8.16 W cm^{-2} was not used for further experiments because the thermochromic sheet is triggered even with a DENV2-NS1-free sample after 10 s of illumination. On the other hand, 5.2 W cm^{-2} is not able to generate a thermochromic signal at low concentrations of DENV2-NS1. The LOD is found at 12.5 ng mL^{-1} when the illumination was performed for 20 s. For the medium power intensity of an LED at 6.5 W cm^{-2}, it allows the detection of DENV2-NS1 at 1.56 ng mL^{-1} as the colour spot was observed on the thermochromic sheet. Therefore, the optimum conditions of illumination were found to be a power intensity of 6.5 W cm^{-2} and 30 s of illumination.

3.5 Sensitivity comparison

Further experiments investigate the sensitivity of DENV2-NS1 detection based on the observation of normal visual and thermochromic signals. The colourations of typical and thermochromic LFA are shown in Fig. 8. For the typical LFA, after the completion of sample migration, only a control line is visible in the absence or short of DENV2-NS1 in the sample, otherwise, the test is invalid. On the other hand, double lines appear on the nitrocellulose membrane indicating a positive result. The test line is observed by the naked eye with confidence at 6.25 ng mL^{-1}, which is the LOD of the typical assay (Fig. 8A).

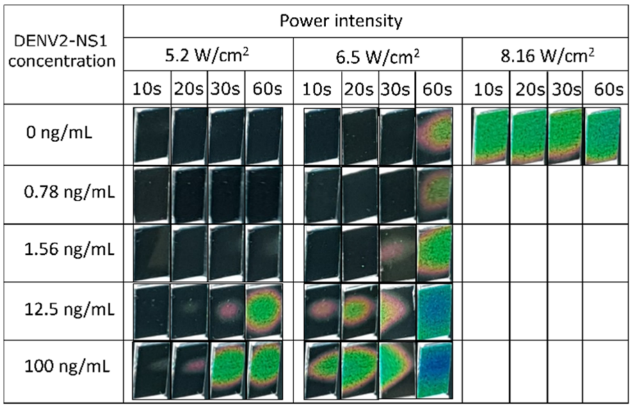

Fig. 7 Thermochromic responses under different conditions. Power intensities are 5.2, 6.5 and 8.16 W cm^{-2} and lengths of exposure are 10, 20, 30 and 60 s. The concentrations of DENV2-NS1 range from 0 to 100 ng mL^{-1}.

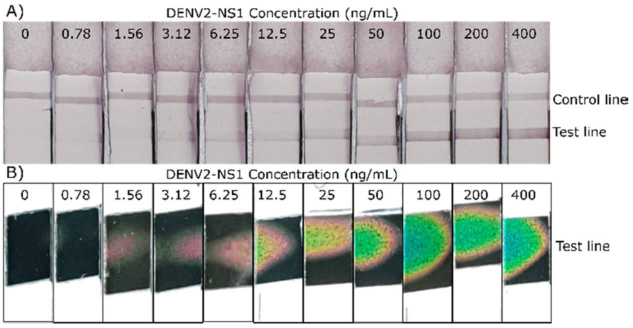

Fig. 8 (A) The strip for typical LFAs and (B) thermochromic sheets of the colorimetric thermal sensing LFA. They were tested against DENV2-NS1 at various concentrations ranging from 0 to 400 ng mL^{-1}.

The low number of analytes in the sample is not able to generate strongly visible test lines. Therefore, instead of directly reading the result, the strip was optically induced to produce heat energy to activate the thermochromic sheet and create a distinct signal. According to Fig. 8B, the method develops an evident red-pink signal at 1.56 ng mL^{-1}. The visual readout of the thermochromic signal reduces the LOD of the LFA by 4 times compared to the conventional LFA. Moreover, it is interesting to note that the colour transition is dependent on the concentration of DENV2-NS1. This finding is in agreement with a previous study that demonstrated the potential to identify the correlation between the thermally induced visual signal and the number of cancer biomarkers.[23] In this study, the minimum temperature activation point is triggered. Subsequently, green and blue pixels grow and spread over the sheet when the concentration of DENV2-NS1 increases. The area of the thermochromic signal expands over the illumination time due to heat map expansion.

Herein, the intensity of the signal was quantified with the assistance of image processing technology. The colour intensity in each pixel of the test line and the thermochromic signal is digitally derived into red, green and blue (RGB) coordinates using a Bayer filter. The contrast between the positive signal and the background was calculated to establish a contrast index for comparison purposes. The colour intensity ratio is an indicator that refers to the test line appearance compared to the background.

The relationship between the concentration of DENV2-NS1 and the intensity ratio is plotted on a log scale as shown in Fig. 9. For the typical colorimetric readout (Fig. 9A–C), the intensity ratio of each colour channel exhibits a similar linear

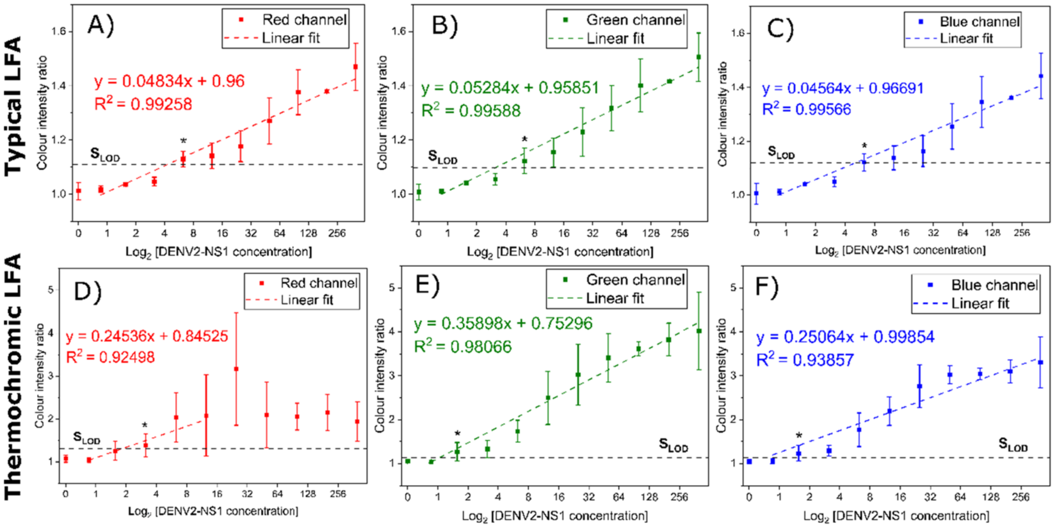

Fig. 9 Logarithm graphs present the relationship between the visual intensity ratios of three primary colours (RGB) and the DENV2-NS1 concentration (0–400 ng mL^{-1}) of typical and thermochromic LFAs: (A–C) typical LFA and (D–F) colorimetric thermal sensing. The * indicates the LOD of that colour channel. Dashed lines are linear trend lines (n = 3).

regression trendline in the range of 0.78 to 400 ng mL^{-1} (R^2 = 0.99258, 0.99588 and 0.99566 for red, green and blue channels, respectively). The green channel is the most sensitive and exhibits the largest intensity signal ratio. A similar finding in the literature when a Bayer filter is used for quantitative analysis of the LFA in which it was suggested that the difference in light scattered by the accumulation of AuNSPs at the test line and the background is most sensitive to the region of the green channel in the Bayer filter.[15] Unlike other thermal sensing LFA formats, the one developed in this study converts heat into a thermochromic signal allowing the quantification of colour intensity. The colour transition of the thermochromic sheet is dependent on the activating temperature resulting in a mixture of primary colour components. The RGB values were obtained from the images used for intensity ratio calculations. In Fig. 9D, the signal intensity ratio of the red channel increases from 1.56 ng mL^{-1} as the red pigment is developed and is locally dominant on the thermochromic sheet. The turning point is found at 25 ng mL^{-1}, as it creates a very large variation before a sharp decrease (R^2 = 0.92498). On the other hand, when the analyte is over 12.5 ng mL^{-1}, the thermochromic sheet develops green and blue pigments while diminishing the red colour, causing a shift in the luminescent region of the Bayer filter. A similar linear trend is observed from 0.78 to 400 ng mL^{-1} for the intensity of the green (Fig. 9E) and blue (Fig. 9F) channels. The R^2 coefficients of the green and blue channels are 0.98066 and 0.93857, respectively. Considering the linear working range, the green and blue channels are more effective for analysis than the red channel. However, the intensity ratio of the green channel offers a slightly larger signal than that of the blue intensity ratio.

The sensitivity and LOD between each Bayer's channel are listed in Table S1.† The acceptable positive signal is the critical value exceeding by at least 3 times the signal of the null concentration sample. Any signals above the level that can be distinguished from the background are treated as positive results. The typical LFA offers the detection limit of DENV2-NS1 at 6.25 ng mL^{-1} for the readout by the naked eye and image analysis. The thermochromic LFA outperforms the typical LFA as it offers greater sensitivity for every colour channel. The LOD of the red channel is 2 times lower than that of the typical LFA but the working range is narrower, hence, the red channel of the thermochromic LFA is ignored. The green and blue channels provide 4-time lower LOD than that of the common LFA. Therefore, considering that the green channel is more sensitive, it is the optimum channel for quantitative analysis.

To facilitate users in terms of readability of the assay, instead of quantification *via* MATLAB software, estimation of the DENV2-NS1 concentration can be conducted by the observation of the colour transition of the thermochromic sheet. In Fig. 10, when the concentration of DENV2-NS1 is below 1.56 ng mL^{-1}, colour transition is not observed. When the concentration of DENV2-NS1 ranges between 1.56 and 12.5 ng mL^{-1}, the red colour appears on the thermochromic sheet. The pres-

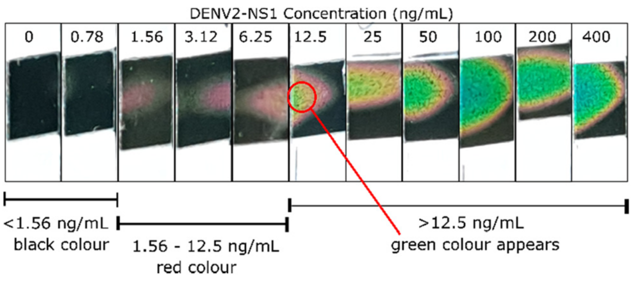

Fig. 10 Semi-quantification method. The concentration range of DENV2-NS1 is represented by the appearance of the colour of the thermochromic sheet.

ence of green colour on the thermochromic sheet is detected when the concentration is over 12.5 ng mL^{-1}. This allows users to quickly estimate the range of DENV2-NS1 concentration without the requirement of an IR camera, a digital temperature sensor, and image processing.

3.6 Discussion

It has been reported that the level of circulating DENV-NS1 in infectious patient serum samples is in the range between 3.64 and 265.7 ng mL^{-1} [6] or 7 and 284 ng mL^{-1}.[36] In the literature, dengue virus can be detected at 4 ng mL^{-1} (ref. 8) and 4.9 ng mL^{-1} (ref. 37) by immunoassay. Tran *et al.* developed a highly sensitive LFA using an enzyme to amplify the signal with the capability of detecting DENV2-NS1 at 0.1 ng mL^{-1}.[38] The median circulating level of DENV2-NS1 was 8.26 ng mL^{-1} from serum samples collected in the first two days after onset of the fever.[6] In children, it is reported that the level of free DENV2-NS1 is approximately 2–2.6 ng mL^{-1} on day 2 of the illness.[39] The developed thermochromic LFA in this study shows a detection limit at 1.56 ng mL^{-1} with a dynamic range from 0.78 to 400 ng mL^{-1}, which covers the range of circulating DENV2-NS1 concentrations found in patients. These data emphasize the potential of using the thermochromic technique in early dengue diagnosis. However, determining the progression of dengue disease depends on the condition of patients, such as primary and secondary infection.[9]

The heat production of nanoparticles (Q, W cm^{-3}) is dependent on the concentration of nanoparticles (N, the number of particles per mL), the absorption cross-sectional area (C, m^2) and the light intensity (I, W m^{-2}):[17]

$$Q = N \times C \times I \tag{3}$$

It is seen that the number of AuNSPs is directly proportional to the extent of heat creation. The higher the concentration of DENV2-NS1, the higher the number of illuminated nanoparticles and the temperature built up.

The orientation of plasmonic particles has great impact on the ability to produce heat. The shorter the distance between each nanoparticle pair, the higher the temperature produced, and *vice versa*.[31] When the concentration of DENV2-NS1 is low, the degree of thermochromic signals from the green and blue channels rises slightly followed by a sharp increase at 12.5 ng mL^{-1} (Fig. 9E and F). This is likely associated with an uneven distribution of AuNSPs throughout the area of the test line, due to the limited number of particles interacting with the test line antibody at low DENV2-NS1 concentration. On the other hand, when the AuNSPs are densely packed, they can produce a higher temperature.

Moreover, the morphology of nanoparticles plays an important role in the photothermal effect because of their different optical properties.[40,41] There are two shapes of gold nanoparticles that were investigated for their heat production, including nanospheres and nanorods, where the absorption spectrum is displayed in Fig. S1B.† The 12 nm nanosphere exhibits the greatest response to the used LED, so it is selected as a light-to-heat converter for the thermal sensing LFA in this study. In theory, the cross-sectional absorption area is directly proportional to photo-thermalization. However, it is applicable for the prediction of a single nanoparticle, but not for nanoparticle clusters in this case.[42] At the same total volume of nanoparticles, the ensemble of small nanoparticles yields a higher temperature than that of the larger one, due to the collective effect.[31,42] Moreover, in terms of heat dissipation, the smaller nanoparticles have less heat capacity than the larger ones, hence they can release excess radiative energy faster and more effectively.[43] Another possible explanation is the enhancement of the scattering effect as the dimension of the nanoparticles increases.[42,43] Re-absorption and re-scattering of light have a vital role in heat production. However, since the nitrocellulose membrane scatters only a partial amount of incident light, and the particles are surrounded by a medium of air, the probability of re-absorption occurring is reduced, and thus a decrease in plasmonic heating was observed.

One of the critical factors to be considered when using the colorimetric thermal sensing LFA, is the domination of ambient temperature. The thermochromic sheet has various working temperature bandwidths as specified by the manufacturer. A necessary step is added to tune the power intensity of light and the illumination time to fit with the ambient temperature to avoid misinterpreting the result.

According to eqn 3, if the concentration and the diameter of AuNSPs are kept constant, the heat production is proportional to the power intensity of illumination. The length of exposure time also needs to be controlled carefully during the operation. The temperature induced by illumination has a tendency to rise over time followed by a steady state at around the maximum temperature. Moreover, the heat can be accumulated and spread over the thermochromic sheet depending on the length of exposure. Prolonging the illumination period can increase the signal, but at the same time, it can cause a false positive result. Therefore, appropriate illumination time and power intensity need to be specifically determined for each application in order not to oversupply photons to the thermal sensing system, otherwise, the thermochromic signal is detectable even in the absence of biological targets.

Thermal sensing measurements usually require background subtraction to eliminate the noise signal. Although the nitrocellulose membrane has poor photothermal effect, light can be absorbed by biological molecules in the membrane resulting in high noise background.[19] Blocking agents are essential to minimize the non-specific binding effect of the nitrocellulose membrane and AuNSP@mAb, nonetheless, they cannot completely remove the undesired noise signal from the system. The use of strong photothermal nanoparticles can potentially solve the problem by creating a massive thermal signal to ensure that the thermochromic signal is far above the noise background signal so that it can be discriminated.[21] The thermochromic sheet can absorb a certain amount of light, leading to a rise of unnecessary temperature attributed to noise. Future work should focus on the use of a filter or a single wavelength light source, or alternative thermally sensitive materials, to eliminate undesirable signals.

4. Conclusion

We have developed a thermochromic paper-based assay for DENV2-NS1 detection. Different types of photothermal nanoparticles were produced for thermal measurements and 12 nm AuNSPs were selected for the development of a thermochromic LFA. Lateral flow strips were quantified by image processing. The thermochromic LFA has a similar linear detection range (0.78–400 ng mL^{-1}) to that of the typical LFA. We found that the thermochromic LFA is significantly more sensitive than the conventional LFA. The test line of the conventional assay is observable at 6.25 ng mL^{-1} whilst the thermochromic signal is visually detectable at 1.56 ng mL^{-1}.

We also demonstrate the possibility of this thermochromic technique for semi-quantitative analysis by simply observing the colour of the thermochromic sheet using a mobile phone camera. This feature does not need image processing analysis and gives a quick result to users. The colour alteration of the thermochromic sheet is observed in the sequence of colours, which correlates to the level of DENV2-NS1 analytes (black = <1.56 ng mL^{-1}, red = 1.56–12.5 ng mL^{-1}, greenish blue = >12.5 ng mL^{-1}).

In conclusion, our thermochromic LFA is a fast, simple, and low-cost technique that offers great sensitivity of the detection of DENV2-NS1 with a wide concentration working range. This can be a promising technique for expanding the utilities of LFA to be used in early clinical diagnosis.

Author contributions

Thithawat Trakoolwilaiwan: methodology, investigation, data analysis, validation, visualisation, and writing – original draft. Yasuhiro Takeuchi: supervision and writing – review and editing. Terence S. Leung: software. Matej Sebek: writing – review and editing. Liudmyla Storozhuk: writing – review and editing. Linh Nguyen: review and editing. Le Duc Tung: writing – review and editing. Nguyen TK Thanh: conceptualisation, data analysis, funding acquisition, project supervision, resources, and writing – review and editing. All authors have read and approved the final manuscript.

Conflicts of interest

There are no conflicts to declare.

Acknowledgements

The authors wish to acknowledge Mark Hassal from NIBSC/MHRA for his advice on antibody and antigen selection. T. T. acknowledges the Royal Thai Government for the PhD studentship and Dr Paul Southern for using a thermal imager. M. S. was funded by the UCL-A*STAR Singapore PhD program. N. T. K. T. thanks the Global Challenges Research Fund for financial support.

References

1 E. E. Ooi and D. J. Gubler, in *Tropical Infectious Diseases: Principles, Pathogens and Practice (Third Edition)*, ed. R. L. Guerrant, D. H. Walker and P. F. Weller, W.B. Saunders, Edinburgh, 2011, pp. 504–510, DOI: 10.1016/B978-0-7020-3935-5.00075-6.

2 C. F. Yung, K. S. Lee, T. L. Thein, L. K. Tan, V. C. Gan, J. G. X. Wong, D. C. Lye, L. C. Ng and Y. S. Leo, *Am. J. Trop. Med. Hyg.*, 2015, **92**, 999–1005.

3 M. G. Guzman, O. Fuentes, E. Martinez and A. B. Perez, in *International Encyclopedia of Public Health (Second Edition)*, ed. S. R. Quah, Academic Press, Oxford, 2017, pp. 233–257, DOI: 10.1016/B978-0-12-803678-5.00103-X.

4 S. Bhatt, P. W. Gething, O. J. Brady, J. P. Messina, A. W. Farlow, C. L. Moyes, J. M. Drake, J. S. Brownstein, A. G. Hoen, O. Sankoh, M. F. Myers, D. B. George, T. Jaenisch, G. R. Wint, C. P. Simmons, T. W. Scott, J. J. Farrar and S. I. Hay, *Nature*, 2013, **496**, 504–507.

5 WHO, *Dengue and severe dengue*, World Health Organization, 2022.

6 S. I. de la Cruz-Hernández, H. Flores-Aguilar, S. González-Mateos, I. López-Martinez, C. Alpuche-Aranda, J. E. Ludert and R. M. del Angel, *Am. J. Trop. Med. Hyg.*, 2013, **88**, 446–454.

7 S. A. Paranavitane, L. Gomes, A. Kamaladasa, T. N. Adikari, N. Wickramasinghe, C. Jeewandara, N. L. Shyamali, G. S. Ogg and G. N. Malavige, *BMC Infect. Dis.*, 2014, **14**, 570.

8 P. R. Young, P. A. Hilditch, C. Bletchly and W. Halloran, *J. Clin. Microbiol.*, 2000, **38**, 1053–1057.

9 S. Chaterji, J. C. Allen Jr., A. Chow, Y. S. Leo and E. E. Ooi, *Am. J. Trop. Med. Hyg.*, 2011, **84**, 224–228.

10 H. Xu, J. Chen, J. Birrenkott, J. X. Zhao, S. Takalkar, K. Baryeh and G. Liu, *Anal. Chem.*, 2014, **86**, 7351–7359.

11 Y. Shen and G. Shen, *ACS Omega*, 2019, **4**, 5083–5087.

12 C. N. Loynachan, M. R. Thomas, E. R. Gray, D. A. Richards, J. Kim, B. S. Miller, J. C. Brookes, S. Agarwal, V. Chudasama, R. A. McKendry and M. M. Stevens, *ACS Nano*, 2018, **12**, 279–288.

13 M. O. Rodríguez, L. B. Covián, A. C. García and M. C. Blanco-López, *Talanta*, 2016, **148**, 272–278.

14 K. Omidfar, F. Khorsand and M. D. Azizi, *Biosens. Bioelectron.*, 2013, **43**, 336–347.

15 J. Park, *Sensors*, 2018, **18**, 4084.

16 W. Lu, K. Wang, K. Xiao, W. Qin, Y. Hou, H. Xu, X. Yan, Y. Chen, D. Cui and J. He, *Sci. Rep.*, 2017, **7**, 42414.

17 Z. Qu, K. Wang, G. Alfranca, J. M. de la Fuente and D. Cui, *Nanoscale Res. Lett.*, 2020, **15**, 10.

18 Y. Wang, Z. Qin, D. R. Boulware, B. S. Pritt, L. M. Sloan, I. J. González, D. Bell, R. R. Rees-Channer, P. Chiodini, W. C. W. Chan and J. C. Bischof, *Anal. Chem.*, 2016, **88**, 11774–11782.

19 L. Zhan, T. Granade, Y. Liu, X. Wei, A. Youngpairoj, V. Sullivan, J. Johnson and J. Bischof, *Microsyst. Nanoeng.*, 2020, **6**, 54.

20 V. Shirshahi, S. N. Tabatabaei, S. Hatamie and R. Saber, *Colloids Surf., B*, 2020, **186**, 110721.

21 X. Hu, J. Wan, X. Peng, H. Zhao, D. Shi, L. Mai, H. Yang, Y. Zhao and X. Yang, *Int. J. Nanomed.*, 2019, **14**, 7695–7705.

22 L. Zheng, W. Dong, C. Zheng, Y. Shen, R. Zhou, Z. Wei, Z. Chen and Y. Lou, *Colloids Surf., B*, 2022, **212**, 112349.

23 E. Polo, P. del Pino, B. Pelaz, V. Grazu and J. M. de la Fuente, *Chem. Commun.*, 2013, **49**, 3676–3678.

24 A. C. Siegel, S. T. Phillips, B. J. Wiley and G. M. Whitesides, *Lab Chip*, 2009, **9**, 2775–2781.

25 M. Nixon, F. Outlaw and T. S. Leung, *PLoS One*, 2020, **15**, e0230561.

26 R. Hachani, M. Lowdell, M. Birchall, A. Hervault, D. Mertz, S. Begin-Colin and N. T. K. Thanh, *Nanoscale*, 2016, **8**, 3278–3287.

27 R. Lévy, N. T. K. Thanh, R. C. Doty, I. Hussain, R. J. Nichols, D. J. Schiffrin, M. Brust and D. G. Fernig, *J. Am. Chem. Soc.*, 2004, **126**, 10076–10084.

28 R. M. Pallares, X. Su, S. H. Lim and N. T. K. Thanh, *J. Mater. Chem. C*, 2016, **4**, 53–61.

29 F. Rossi, E. H. Khoo, X. Su and N. T. K. Thanh, *ACS Appl. Bio Mater.*, 2020, **3**, 315–326.

30 Á. Lavín, J. D. Vicente, M. Holgado, M. F. Laguna, R. Casquel, B. Santamaría, M. V. Maigler, A. L. Hernández and Y. Ramírez, *Sensors*, 2018, **18**, 2038.

31 A. O. Govorov and H. H. Richardson, *Nano Today*, 2007, **2**, 30–38.

32 C. Parolo, A. de la Escosura-Muñiz, E. Polo, V. Grazú, J. M. de la Fuente and A. Merkoçi, *ACS Appl. Mater. Interfaces*, 2013, **5**, 10753–10759.

33 N. G. Welch, J. A. Scoble, B. W. Muir and P. J. Pigram, *Biointerphases*, 2017, **12**, 02d301.

34 S. Zhang, Y. Moustafa and Q. Huo, *ACS Appl. Mater. Interfaces*, 2014, **6**, 21184–21192.

35 N. A. Byzova, I. V. Safenkova, E. S. Slutskaya, A. V. Zherdev and B. B. Dzantiev, *Bioconjugate Chem.*, 2017, **28**, 2737–2746.

36 D. Allonso, M. D. Meneses, C. A. Fernandes, D. F. Ferreira and R. Mohana-Borges, *PLoS One*, 2014, **9**, e113634.

37 S. Kumar, P. Bhushan, V. Krishna and S. Bhattacharya, *Biomicrofluidics*, 2018, **12**, 034104–034104.

38 T. V. Tran, B. V. Nguyen, T. T. P. Nguyen, T. T. Tran, K. G. Pham, Q. B. Le, B. N. Do, H. N. Pham, C. V. Nguyen, D. P. H. Dinh, V. T. Ha, T. H. T. Doan and H. Q. Le, *PeerJ*, 2019, **7**, e7779.

39 D. H. Libraty, P. R. Young, D. Pickering, T. P. Endy, S. Kalayanarooj, S. Green, D. W. Vaughn, A. Nisalak, F. A. Ennis and A. L. Rothman, *J. Infect. Dis.*, 2002, **186**, 1165–1168.

40 H. Zakaria, W. S. Abdelaziz and T. Youssef, *Lasers Med. Sci.*, 2016, **31**, 625–634.

41 G. Baffou, R. Quidant and C. Girard, *Appl. Phys. Lett.*, 2009, **94**, 153109.

42 S. M. Meyer, J. Pettine, D. J. Nesbitt and C. J. Murphy, *J. Phys. Chem. C*, 2021, **125**, 16268–16278.

43 R. K. Kashyap, M. J. Parammal and P. P. Pillai, *ChemNanoMat*, 2022, **8**, e202200252.